How to cite: *Angew. Chem. Int. Ed.* **2021**, *60*, 13484–13492
International Edition: doi.org/10.1002/anie.202103353
German Edition: doi.org/10.1002/ange.202103353

**Nanosheets**

# Covalent Bisfunctionalization of Two-Dimensional Molybdenum Disulfide

*Xin Chen, Cian Bartlam, Vicent Lloret, Narine Moses Badlyan, Stefan Wolff, Roland Gillen, Tanja Stimpel-Lindner, Janina Maultzsch, Georg S. Duesberg, Kathrin C. Knirsch, and Andreas Hirsch**

***Abstract:*** *Covalent functionalization of two-dimensional molybdenum disulfide (2D $MoS_2$) holds great promise in developing robust organic-$MoS_2$ hybrid structures. Herein, for the first time, we demonstrate an approach to building up a bisfunctionalized $MoS_2$ hybrid structure through successively reacting activated $MoS_2$ with alkyl iodide and aryl diazonium salts. This approach can be utilized to modify both colloidal and substrate supported $MoS_2$ nanosheets. We have discovered that compared to the adducts formed through the reactions of $MoS_2$ with diazonium salts, those formed through the reactions of $MoS_2$ with alkyl iodides display higher reactivity towards further reactions with electrophiles. We are convinced that our systematic study on the formation and reactivity of covalently functionalized $MoS_2$ hybrids will provide some practical guidance on multi-angle tailoring of the properties of 2D $MoS_2$ for various potential applications.*

## Introduction

Two-dimensional transition metal dichalcogenides (2D TMDs) are in the spotlight of nanomaterial community in the last decade since they have shown great potential in a variety of areas such as electronic/optoelectronic devices,[1–3] catalysis,[4–6] sensing,[7–9] and biomedical applications.[10–12] A lot of research projects has been concentrated on the development of methods to controllably produce TMD nanosheets.[2,13–16] These methods enable the production of 2D TMDs with customizable size, thickness, and spatial orientations, encouraging the deep investigation of fundamental physics and chemistry of TMD nanosheets. In the meantime, the research topics on chemical functionalization of 2D TMDs, through either covalent or non-covalent approaches, have flourished.[17–21] This has enabled further tailoring of properties, control over processability, and improved versatility of TMD based material applications, facilitating the fulfillment of the potential of 2D TMDs.

As a prototype of 2D TMDs, 2D $MoS_2$ is extensively used as a model system to explore the functionalization chemistry of TMDs. Compared to non-covalent functionalization, covalent functionalization shows particular advantages in terms of the robustness of formed conjugates,[22] the efficiency of electronic communication at the functional groups/$MoS_2$ interface,[23] and the versatility endowed by the variety of functional groups.[22,24–25] Recently, Knirsch et al.[17] and Voiry et al.[18] have demonstrated protocols to covalently functionalize chemically exfoliated $MoS_2$ (*ce*-$MoS_2$) nanosheets using either diazonium salts or organohalides (-I or -Br). By virtue of these two approaches, a library of covalently functionalized $MoS_2$-organic/inorganic hybrid structures have been generated.[26–28] Among all of these reported covalent hybrids, almost all of the materials are monofunctionalized, in which only one type of functional group is grafted onto $MoS_2$. One step further, the incorporation of multiple and diverse functionalities into 2D $MoS_2$ would enable the integration of multiple functionalities of different surface addends into one device, opening the opportunity to achieve a smart nanomachine with tailor-made properties and integrated functions. In this respect, the development of such a functionalized $MoS_2$ hybrid structure bearing two or multiple covalently tethered functionalities is highly desired.

Additionally, we note that the reactions of $MoS_2$ nanosheets with organohalides have shown some distinct phenomena compared to those with diazonium salts. For example, the functionalization of 2D $MoS_2$ with organohalides has only been achieved so far using 1T-phase *ce*-$MoS_2$ nanosheets[18] but not 2H-$MoS_2$ (unless with a catalyst),[25] whereas the arylation of 2D $MoS_2$ using diazonium salts can be realized by either 1T- phase *ce*-$MoS_2$[17] or 2H-phase $MoS_2$ nanosheets (prepared by mechanical exfoliation or chemical vapor deposition).[27] Secondly, the treatment of negatively charged 1T-phase *ce*-$MoS_2$ with organohalides leads to partial charge neutralization,[28] while the treatment of *ce*-$MoS_2$ with diazonium salts leads to complete charge neutralization.[17] Many

[*] Dr. X. Chen, V. Lloret, Dr. K. C. Knirsch, Prof. A. Hirsch
Department of Chemistry and Pharmacy, Friedrich-Alexander-Universität (FAU) Erlangen-Nürnberg
Nikolaus-Fiebiger-Strasse 10, 91058 Erlangen (Germany)
E-mail: andreas.hirsch@fau.de
Dr. C. Bartlam, Dr. T. Stimpel-Lindner, Prof. G. S. Duesberg
Institute of Physics, Faculty of Electrical Engineering and Information Technology, Universität der Bundeswehr München
Werner-Heisenberg-Weg 39, 85577 Neubiberg (Germany)
N. Moses Badlyan, S. Wolff, Dr. R. Gillen, Prof. J. Maultzsch
Department of Physics, Friedrich-Alexander-Universität (FAU) Erlangen-Nürnberg
Staudtstrasse 7, 91058 Erlangen (Germany)
Supporting information and the ORCID identification number(s) for the author(s) of this article can be found under: https://doi.org/10.1002/anie.202103353.

aspects regarding the chemistry of covalent functionalization of $MoS_2$ nanosheets using these two types of electrophiles are not fully understood yet.

In this study, we demonstrate an approach to construct a bisfunctionalized $MoS_2$ hybrid structure bearing both alkyl and aryl groups. These two types of functional groups were covalently tethered onto $MoS_2$ through the successive reaction of chemically activated $MoS_2$ with alkyl iodides and aryl diazonium salts. By adjusting the functionalization sequence and carefully analyzing the reaction intermediates and final adducts using a series of spectroscopic and microscopic techniques, we shed light on the fundamental aspects of covalent functionalization chemistry of 2D $MoS_2$.

## Results and Discussion

### Synthesis of bisfunctionalized $MoS_2$

The bisfunctionalized 2D $MoS_2$ was synthesized using a stepwise approach, starting with the preparation of $MoS_2$ nanosheets via chemical exfoliation. Specifically, bulk $MoS_2$ powder was initially reacted with *n*-BuLi followed by the hydration and sonication of the intercalated compound in water, as detailed in previous literature.[13,22] Then, the freshly prepared and purified *ce*-$MoS_2$ was reacted with iodohexane (electrophile A) in a manner analogous to the reported procedure,[18] giving the alkylated intermediate product *A*-$MoS_2$. After purification, *A*-$MoS_2$ was re-dispersed in isopropanol and reacted with 4-bromobenzenediazonium tetrafluoroborate (electrophile B) to form the final product *AB*-$MoS_2$. Alternatively, the two-step functionalization was also performed by following the reverse order, in which *ce*-$MoS_2$ was firstly reacted with 4-bromobenzenediazonium tetrafluoroborate (electrophile B),[17] yielding the arylated intermediate product *B*-$MoS_2$. The subsequent reaction of *B*-$MoS_2$ with iodohexane (electrophile A) gave the product *BA*-$MoS_2$ (Scheme 1, see the Supporting Information for details).

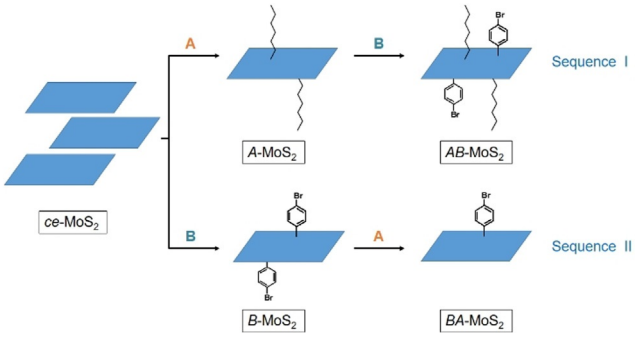


***Scheme 1.*** Illustration of the functionalization sequence I and II. Reagent A: iodohexane. Reagent B: 4-bromobenzenediazonium tetrafluoroborate. Sequence I, alkylation followed by arylation, leads to the formation of bisfunctionalized adduct *AB*-$MoS_2$. Sequence II, arylation followed by alkylation, can only give the monofunctionalized product *BA*-$MoS_2$. The structural differences between *B*-$MoS_2$ and *BA*-$MoS_2$ are illustrated in the following context.

### Characterization

To identify the nature and the content of functional groups, the as-prepared *ce*-$MoS_2$, *A*-$MoS_2$, *B*-$MoS_2$, *AB*-$MoS_2$, and *BA*-$MoS_2$ were analyzed by thermogravimetric analysis coupled with mass spectrometry (TGA-MS). *ce*-$MoS_2$ (Figure S1a) displays a gradual thermal decomposition starting from 200 °C with a total mass loss of 5 % at $T = 700$ °C, which was attributed to the degradation of $MoS_2$ itself. In comparison, TGA-MS profile of *A*-$MoS_2$ (Figure S1b) shows a total mass loss of 8 % over the same temperature range with the maximum ion current detected at 275 °C. The major gaseous products were identified with the $m/z$ of 55, 43, and 41, corresponding to the hexyl group related fragments $C_4H_7^+$, $C_3H_7^+$, and $C_3H_5^+$, respectively, suggesting that hexyl groups are present in *A*-$MoS_2$. Thermolysis of *B*-$MoS_2$ (Figure S1c) reveals a mass loss of 20 % with the maximum ion current detected at 410 °C. The dominant ion currents are found to be the fragments $C_6H_5^+$ ($m/z = 77$) and $C_6H_6$ ($m/z = 78$) associated with the aryl moiety, suggesting the presence of phenyl groups in *B*-$MoS_2$.

Interestingly, the final hybrid product from sequence I, *AB*-$MoS_2$ (Figure 1a), exhibits a mass loss of 19 %, much higher than that of the intermediate product *A*-$MoS_2$ (8 %), suggesting that a higher content of functional groups are present in *AB*-$MoS_2$ compared to *A*-$MoS_2$. The major gaseous products from thermal decomposition of *AB*-$MoS_2$ were detected with $m/z = 43$ and 77, corresponding to the characteristic fragments of hexyl group and phenyl group, respectively. This result demonstrates the successful introduction of both hexyl and phenyl groups in *AB*-$MoS_2$. In contrast, the final product from sequence II, *BA*-$MoS_2$ (Figure 1b), shows a total mass loss of 17 %, slightly lower than that of the intermediate product *B*-$MoS_2$ (20 %). In addition, the dominant ion current was detected as the phenyl group related fragment $C_6H_5^+$ ($m/z = 77$), suggesting that phenyl groups remain present in *BA*-$MoS_2$. However, the hexyl group related fragment ($C_3H_5^+$, $m/z = 43$) was detected in a small amount and at low temperature region. This implies that only a trace amount of hexyl group related species is present in *BA*-$MoS_2$, which was presumably physisorbed on the $MoS_2$ surface.

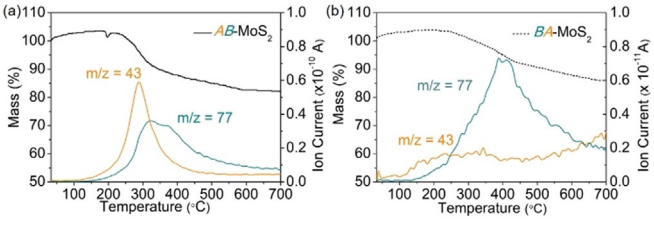


***Figure 1.*** TGA-MS profiles (black) of *AB*-$MoS_2$ (a) and *BA*-$MoS_2$ (b). The ion currents in *AB*-$MoS_2$ and *BA*-$MoS_2$ are the fragment $C_3H_7^+$ ($m/z$ 43, orange trace) derived from the decomposed hexyl group and the fragment $C_6H_5^+$ ($m/z$ 77, cyan trace) associated with the aryl group. The small amount of fragment $C_3H_7^+$ detected in *BA*-$MoS_2$ at low temperature range originates from the detachment of physisorbed alkyl groups.

  

The Fourier-transform infrared spectroscopy (FT-IR) measurement of *AB*-$MoS_2$ (Figure S2, red trace) demonstrates strong absorption peaks in the range of 3000–2840 $cm^{-1}$ and 1760–1000 $cm^{-1}$, which are attributed to vibrational features of alkyl chain and aromatic ring, respectively; whereas *BA*-$MoS_2$ (Figure S2, blue trace) shows almost identical features to the arylated intermediate *B*-$MoS_2$ (Figure S2, dark cyan trace). The alkyl chain related peaks with very low intensity were discernable in the FT-IR spectra of *BA*-$MoS_2$ (Figure S2, blue trace), which were presumably derived from the physisorbed alkyl moieties. This is in a good agreement with TGA-MS results.

To further investigate the chemical state and quantify the elemental composition of *ce*-$MoS_2$ and functionalized materials, high resolution X-ray photoelectron spectroscopy (XPS) analysis was carried out. The elemental analysis of survey spectra (see Table S1 for the detailed elemental composition) shows the presence of Br (Br 3d, 70 eV) in *B*-$MoS_2$, *AB*-$MoS_2$, and *BA*-$MoS_2$, suggesting the successful incorporation of bromophenyl functional groups in these three samples. No N related signals were detected in functionalized $MoS_2$, confirming that the unreacted 4-bromobenzenediazonium salts are not present in the functionalized samples and the functionalization reaction likely proceeds via the substitution of the diazo groups. Further comparison of *BA*-$MoS_2$ with *B*-$MoS_2$ reveals a negligible change of C and Br content (Table S2), suggesting that the degree of functionalization is likely the same. Additionally, the atomic percentages of C and Br were found to significantly increase in *AB*-$MoS_2$ relative to *A*-$MoS_2$, indicating the successful introduction of bromophenyl group in *AB*-$MoS_2$ through the second step functionalization. This coincides with our TGA-MS results.

Fitting the Mo 3d core level spectra by deconvolution allows us to determine the concentration of 1T- and 2H-phase in each sample. The Mo 3d core level spectra of *ce*-$MoS_2$ and functionalized $MoS_2$ can be fitted with three sets of doublets, which are attributed to the Mo $3d_{3/2}$ and Mo $3d_{5/2}$ components of 2H-$MoS_2$, 1T-$MoS_2$, and $MoO_3$ (Figure 2 a–e). The content of 1T- phase was found to be 19% in *ce*-$MoS_2$, whereas this was approximately 60–70% in the functionalized $MoS_2$. The lower concentration of 1T-phase in *ce*-$MoS_2$ can be ascribed to aging effects during the sample delivery and storage, which has been proved to cause phase rearrangement from 1T to 2H.[17–18,29] In comparison, the large proportion of 1T-phase in the functionalized $MoS_2$ suggests that the 1T-phase was largely preserved after functionalization. Furthermore, the continuing functionalization of the intermediate did not alter the concentration of 1T-phase, which is evidenced by the similar content of 1T-phase in *AB*-$MoS_2$ relative to *A*-$MoS_2$ and likewise in *BA*-$MoS_2$ relative to *B*-$MoS_2$ (Table S2, content of 1T-phase in all the samples). This is important, because it demonstrates that the concentration of 1T-phase can be stabilized against the conversion back to 2H-phase through functionalization.

We performed DFT calculations (see supporting information for details) in order to get a better understanding of the phase composition in functionalized $MoS_2$. Starting with $2\times2$ 1T-$MoS_2$ and 2H-$MoS_2$ unit cells and placing one functional group 2 Å above the $MoS_2$ layer, this results in a 25% coverage of one side of the layer. For 1T-$MoS_2$ (octahedral coordination), the calculations indicate a phase transition to a distorted octahedral coordination (also referred to as 1T′-phase). This suggests that the 1T-phase, which is thermodynamically metastable, is stabilized upon covalent functionalization, and the slight lattice distortion helps to maintain the octahedral coordination in functionalized $MoS_2$ structures. This result corroborates our observations in XPS measurements. For 2H-$MoS_2$ (trigonal prismatic coordination), the structure is preserved when adding the functional group. These effects are observed independently of the type of attached functional groups.

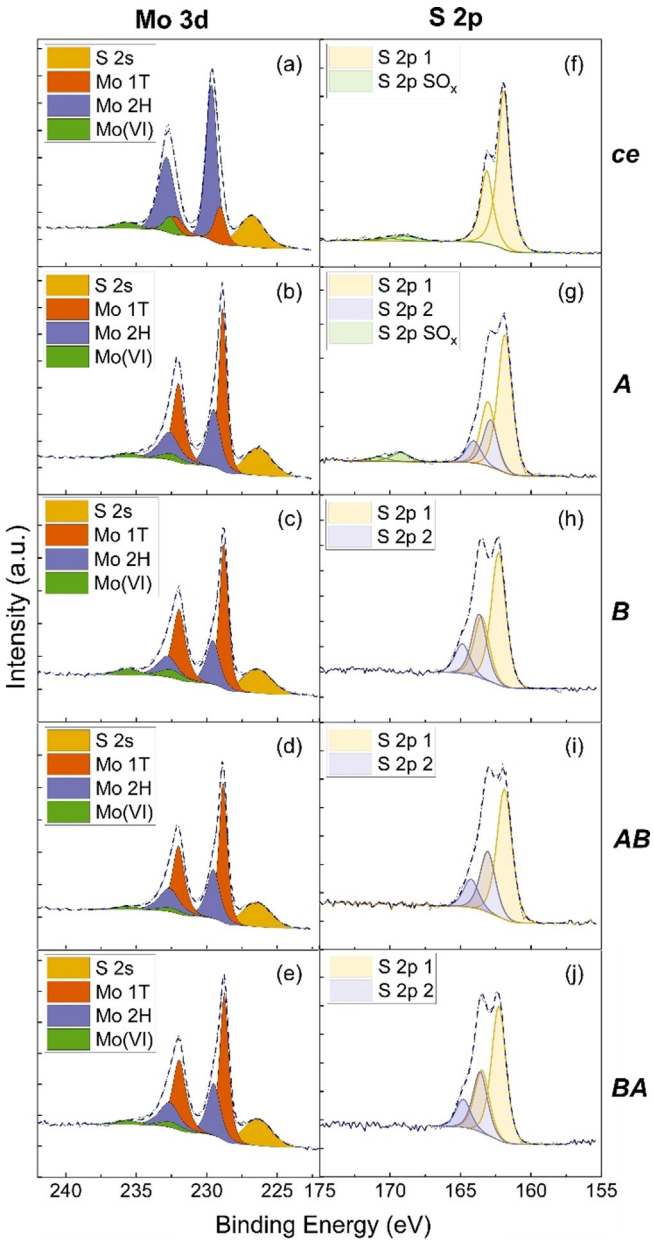


***Figure 2.*** XPS core level spectra of Mo 3d (a–e) and S 2p (f–j) for *ce*-$MoS_2$, *A*-$MoS_2$, *B*-$MoS_2$, *AB*-$MoS_2$, and *BA*-$MoS_2$. The orange component in (a–e) can be attributed to the S 2s peak, which heavily overlaps with Mo 3d components. The green components in (f) and (g) can be assigned to oxidized sulfur species.

  

To determine the degree of functionalization, we closely inspected the S 2p core level spectra. In addition to the typical doublet feature (yellow components, Figure 2 f–j) corresponding to the S $2p_{3/2}$ (161.9 eV) and S $2p_{1/2}$ (163.1 eV) components of $MoS_2$, the S 2p spectra of *A*-$MoS_2$, *B*-$MoS_2$, *AB*-$MoS_2$, and *BA*-$MoS_2$ display a shoulder at 164.45 ± 0.02 eV (purple components, Figure 2 f–j), which is usually assigned to the C-S species derived from covalent functionalization.[17,23] The degree of covalent functionalization (functional groups per S), calculated based on the peak area underneath of this C-S component relative to the total area of S 2p, was found to be 24 %, 32 %, 31 %, and 31 % for *A*-$MoS_2$, *B*-$MoS_2$, *AB*-$MoS_2$, and *BA*-$MoS_2$, respectively.

Compared to *A*-$MoS_2$, *AB*-$MoS_2$ shows a higher degree of functionalization, which is consistent with the TGA-MS analysis. The higher content of functional groups in *AB*-$MoS_2$ relative to *A*-$MoS_2$ is attributed to the successful introduction of aryl functional groups through the second step functionalization which is further seen based on the Br concentration in the survey spectra (Table S1). In comparison, *BA*-$MoS_2$ displays almost same degree of functionalization to *B*-$MoS_2$. This is consistent with the observation in XPS survey analysis. Interestingly, the maximum degree of functionalization after two-step successive functionalization reaches about 30 % regardless of the reaction sequences. In addition, the functionalization of activated $MoS_2$ using organoiodides leads to a lower degree of functionalization compared to that using diazonium salts, indicating that the latter is more efficient.

For further exploration of the chemical identity and the binding sites of functional groups, *A*-$MoS_2$, *B*-$MoS_2$, *AB*-$MoS_2$, and *BA*-$MoS_2$ were investigated using solid state $^{13}C$ (126 MHz) magic angle spinning nuclear magnetic resonance spectroscopy (MAS NMR, Figure 3 and S3). The $^{13}C$ NMR spectrum of iodohexane (Figure S3a) displays six singlet signals in the range of 5–35 ppm, corresponding to the aliphatic carbons of hexyl chain. In particular, the characteristic signal at $\delta = 7.27$ ppm corresponds to the α-C connected to iodine. In comparison, *A*-$MoS_2$ (Figure S3b) shows three sets of widened signals in the range of 10–35 ppm, demonstrating the presence of aliphatic carbons associated with the hexyl chain. The dramatically broadening of signals in the solid state sample probably hinges on the anisotropy, orientation or magnetic susceptibility effects arising from the charged nanosheets.[30–31] Most importantly, the signal related to the α-C is absent from the original chemical shift region, suggesting that this α-C was involved in the functionalization reaction between iodohexane and $MoS_2$. The α-C related peak is shifted downfield and thus, jointly with other aliphatic carbons, constitute the prominent signals in *A*-$MoS_2$. This downfield shift of α-C also suggests a de-shielding effect, which was presumably caused by the formation of bonds between α-C atoms and more electronegative atoms (in this case the sulfur atoms) through coupling iodohexane to $MoS_2$. The formation of C–S bonds is in accord with our results in the XPS S2p core level spectra, corroborating that hexyl groups were tethered to the S atoms of $MoS_2$ in *A*-$MoS_2$. Similar observations have been reported in other alkyl functionalized $MoS_2$ systems.[18]

Analogous analysis was also performed on 4-bromothiophenol reference (Figure S3c) and *B*-$MoS_2$ (Figure S3d). In this case, the characteristic signal corresponding to the aromatic carbons of the bromophenyl group was observed in *B*-$MoS_2$, verifying the presence of these groups. The resonances of aromatic carbons in *B*-$MoS_2$ are centered at the similar chemical shift to that of bromothiophenol, suggesting that a similar electronic environment of aromatic ring is maintained by the functional groups in *B*-$MoS_2$ relative to bromothiophenol. We only observed a slight downfield shift of δ-C (-$CH_{aromatic}$-Br) in *B*-$MoS_2$, which was likely due to the variation of C-S bond strength at the interface of $MoS_2$ and bromophenyl functional groups compared to that between thiol group (SH) and bromophenyl moiety in bromothiophenol. Nevertheless, the solid state NMR analysis confirmed the covalent attachment of alkyl and aryl functional groups in *A*-$MoS_2$ and *B*-$MoS_2$, respectively.

Further comparison of the $^{13}C$ solid state NMR spectra for *A*-$MoS_2$, *B*-$MoS_2$, and *AB*-$MoS_2$ (Figure 3 a–c) reveals the characteristic shifts corresponding to the aliphatic and aromatic carbons, demonstrating that both hexyl and bromophenyl functional groups were covalently bound to the S-atoms of $MoS_2$ in *AB*-$MoS_2$. In contrast, *BA*-$MoS_2$ (Figure 3 d) shows similar features to *B*-$MoS_2$, where the major signal is derived from the covalently tethered aromatic carbon moieties. It is noted that a few peaks with very low intensities can be distinguished, which show characteristic features of iodohexane, for example, α-C (-$CH_2$-I) was detected, but not the covalently tethered hexyl chain, suggesting the presence of trace amounts of physisorbed iodohexane in *BA*-$MoS_2$, in good agreement with our TGA-MS and FT-IR results.

The morphology of $MoS_2$ nanosheets before and after functionalization was examined using scanning electron microscopy (SEM) at different magnification scales. The SEM images (Figure 4 a and f) of *ce*-$MoS_2$ show characteristic layered structures with diverse lateral sizes and well-defined edges. The features of the nanoflakes are well preserved in *A*-

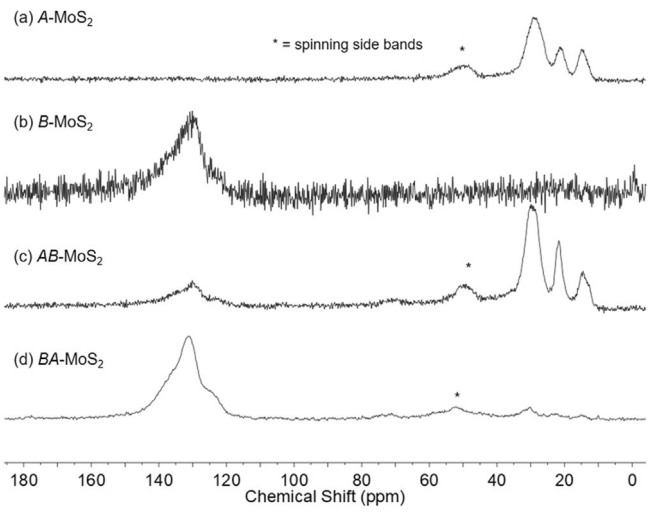


***Figure 3.*** $^{13}C$ solid-state NMR spectra of *A*-$MoS_2$ (a), *B*-$MoS_2$ (b), *AB*-$MoS_2$ (c), and *BA*-$MoS_2$ (d). All the samples were spun at 14 kHz except for *BA*-$MoS_2$, which was spun at 10 kHz.

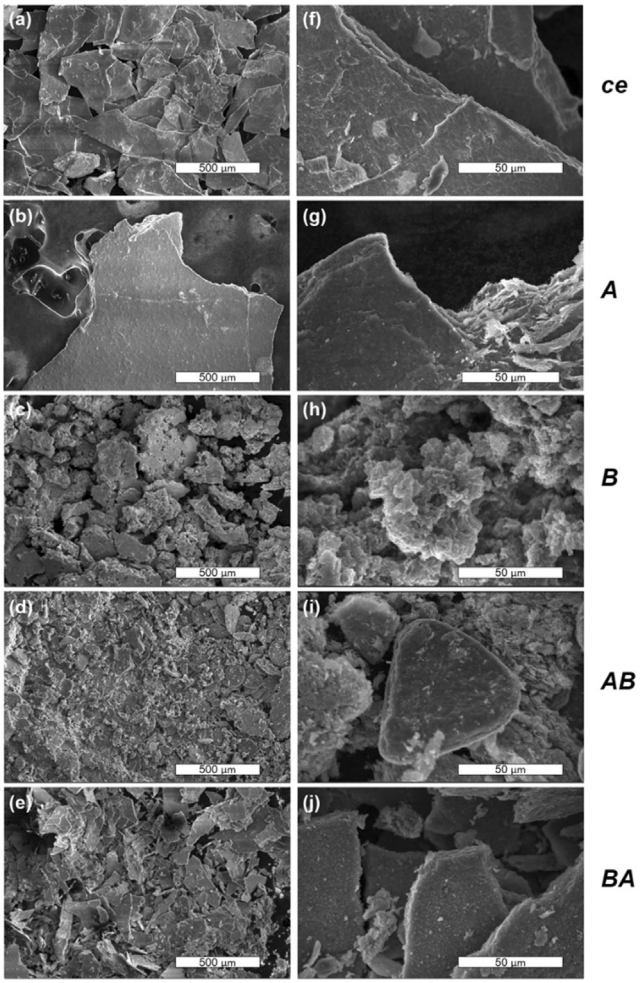


***Figure 4.*** SEM images of *ce*-$MoS_2$ (a), *A*-$MoS_2$ (b), *B*-$MoS_2$ c), *AB*-$MoS_2$ (d), and *BA*-$MoS_2$ (e) and corresponding views (f–j) under higher magnification.

$MoS_2$ (Figure 4b and g) with relatively more disrupted edges compared to *ce*-$MoS_2$. This can be a sign of chemical modification via the reaction with iodohexane. The morphology of *B*-$MoS_2$ (Figure 4c and h) is strikingly different from either *ce*-$MoS_2$ or *A*-$MoS_2$, where instead of a layered structure, amorphous chunks were observed. This is likely attributed to the formation of oligomer during the functionalization reaction, in which the excess aryl radicals can either attach to the surface tethered aryl groups, forming the oligomer layers, or react with each other via biaryl coupling to form aryl oligomers prior to covalently bonding to the $MoS_2$ surface. These side reactions have been reported in the reactions between diazonium salts and graphene.[32–33] The dramatic change in morphology of *B*-$MoS_2$ indicates a transformative change in the surface properties upon functionalization using diazonium salts. Despite the fact that covalent functionalization of $MoS_2$ nanosheets using diazonium salts has been extensively applied in recent years,[17,23,27] this is the first time that covalent functionalization induced morphology change is reported and outlined. Our finding can provide a new perspective to fundamentally understand the dramatic variation in the properties of materials functionalized using diazonium chemistry, when compared to their parental $MoS_2$ nanosheets. This effect can also be distinctly observed when comparing the morphology of intermediate product *A*-$MoS_2$ (Figure 4b and g) with bisfunctionalized product *AB*-$MoS_2$ (Figure 4d and i). The layered structure shown in *A*-$MoS_2$ was transformed into a fragmented and petal-like structure in *AB*-$MoS_2$ after the functionalization with diazonium salts.

Further inspection of the SEM images of *BA*-$MoS_2$ (Figure 5e and j) reveals features of the nanoflakes with much smaller lateral sizes compared to *ce*-$MoS_2$. Our previous TGA-MS, FT-IR and XPS results have indicated that the second-step reaction of *B*-$MoS_2$ with 1-iodohexane failed to covalently attach alkyl groups to $MoS_2$. The degree of covalent functionalization remained same in *B*-$MoS_2$ and *BA*-$MoS_2$. We then deduced that the recovery of layered structure in *BA*-$MoS_2$ was possibly attributed to the removal of amorphous oligomer layers in highly functionalized *B*-$MoS_2$.

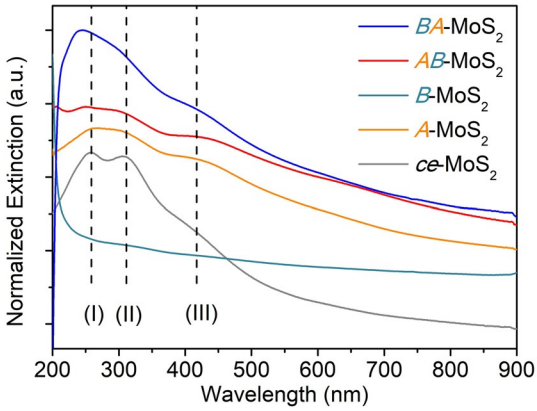


***Figure 5.*** Extinction spectra of *ce*-$MoS_2$ (grey), *A*-$MoS_2$ (orange), *B*-$MoS_2$ (cyan), *AB*-$MoS_2$ (red), and *BA*-$MoS_2$ (blue). The dashed lines indicate the bands discussed in the following context. The spectra were normalized to the maximum intensity for comparison.

We then performed energy dispersive X-ray (EDS) mapping of all of the samples (Table S3 for detailed elemental composition). In addition to the uniformly distributed Mo and S signals, the Br signal was detected in *B*-$MoS_2$, *AB*-$MoS_2$, and *BA*-$MoS_2$, verifying the presence of bromophenyl functional groups in these samples. Moreover, the atomic percentage of Br slightly dropped in *BA*-$MoS_2$ compared to *B*-$MoS_2$, which could be due to the removal of Br-containing moieties (e.g. oligomers) during the second step treatment. These observations show good agreement with our XPS results.

### *Optical properties*

Having determined the chemical nature of the functionalized $MoS_2$, we then set out to monitor how the functionalization affects the optical properties of $MoS_2$ nanosheets. The extinction spectra (Figure 5) of *ce*-$MoS_2$ and functionalized $MoS_2$ display intense bands in the ultra-violet region

  

except for *B*-$MoS_2$ (dark cyan trace in Figure 5), in which the excitonic transitions were virtually quenched. This is possibly due to the complete change in morphology of *B*-$MoS_2$ in comparison to the others. Interestingly, the excitonic transition bands were recovered in *BA*-$MoS_2$ (blue trace in Figure 5), which was not surprising as the recuperation of $MoS_2$ layered structure after the second step reaction was observed in our SEM study (Figure 5e and j). Similar observations have been reported for other $MoS_2$ based materials, which were functionalized using diazonium chemistry as well.[17]

To closely inspect the peak positions of the bands in the ultra-violet region, we plotted the second derivative of extinction spectra (Figure S4a). Three distinct bands can be identified in *ce*-$MoS_2$: band (I) at 246 nm, band (II) at 317 nm, and band (III) at 417 nm. These bands are all preserved in *A*-$MoS_2$ and *AB*-$MoS_2$, while only band (II) and (III) are present in *B*-$MoS_2$ and *BA*-$MoS_2$. The disappearance of band (I) in *B*-$MoS_2$ and *BA*-$MoS_2$ demonstrates the dramatic change in electronic properties in these two samples. The position of band (III) is located in the visible region and close to where C exciton of $MoS_2$ is, thus is indicative of the presence of 2H-phase in all samples, which is consistent with our XPS observations. In addition, band (III) is up-shifted in all functionalized samples compared to *ce*-$MoS_2$, which could be ascribed to increased scattering effects arising from re-aggregation.[22,34–35] Interestingly, in comparison to *ce*-$MoS_2$, we observed down-shift of band (II) in *A*-$MoS_2$, *AB*-$MoS_2$, and *BA*-$MoS_2$, but up-shift in *B*-$MoS_2$. The morphology of *B*-$MoS_2$ is totally different from the others, which brings some complexity to analyzing the change of electronic bands of *B*-$MoS_2$. Herein, we will only discuss the shift of band (II) with respect to the other samples (Figure S4b, red plot). The magnitude of the down-shift follows the order: *A*-$MoS_2$ < *AB*-$MoS_2$ < *BA*-$MoS_2$, indicating that the more bromophenyl groups tethered on the surface, the more significant the change imparted onto the electronic structure of $MoS_2$.

To further elucidate the influence of covalent functionalization on the optical properties of $MoS_2$, the dispersions of *ce*-$MoS_2$, *A*-$MoS_2$, *B*-$MoS_2$, *AB*-$MoS_2$, and *BA*-$MoS_2$ were deposited on $Si/SiO_2$ wafers via spin-coating to form thin films and measured by scanning Raman spectroscopy under resonant excitation ($\lambda = 633$ nm) at room temperature (Figure 6a). The average spectrum calculated from 121 recorded single point spectra was analyzed for each sample. The Raman spectrum of *ce*-$MoS_2$ shows characteristic peaks of $MoS_2$ at 377, 406, and 450 $cm^{-1}$, corresponding to $E^1_{2g}$, $A_{1g}$, and 2LA(M),[36] respectively. In addition, a series of features at lower frequencies was detected, among which the features at 150, 223 and 326 $cm^{-1}$ are assigned to 1T-phase related $J_1$–$J_3$ modes,[37] and the peak at 188 $cm^{-1}$ is identified as the two-phonon difference combination mode $A_{1g}$(M)-LA(M).[36] The Raman spectra of the functionalized samples display almost all of the key features of $MoS_2$ with decreasing peak intensity and an increase in peak widths compared to *ce*-$MoS_2$, suggesting reduced $MoS_2$ crystallinity after functionalization. There is no significant shift of the frequencies of characteristic Raman modes of $MoS_2$ after functionalization. In addition, the $J_1$ and $J_2$ modes are still present in the functionalized

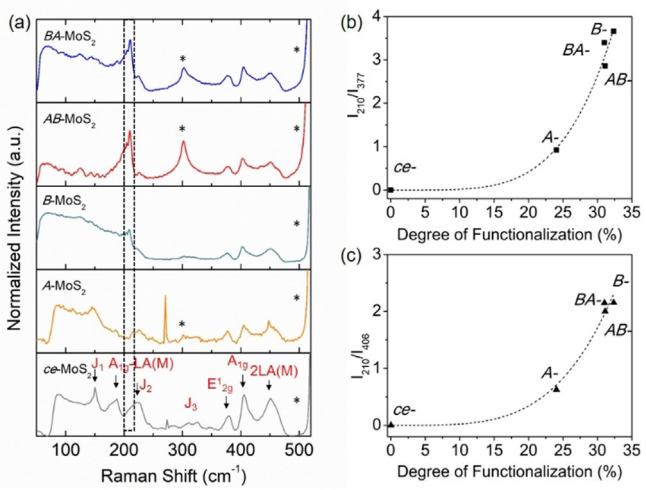


***Figure 6.*** Raman spectra a) of *ce*-$MoS_2$ (grey), *A*-$MoS_2$ (orange), *B*-$MoS_2$ (cyan), *AB*-$MoS_2$ (red), and *BA*-$MoS_2$ (blue): the arrows show the characteristic Raman scattering of *ce*-$MoS_2$; the dashed block highlights the emerging peak at 210 $cm^{-1}$, the peaks marked with an asterisk are Raman modes of the underlying $Si/SiO_2$ substrate. The sharp peak at around 270 $cm^{-1}$ in *ce*-$MoS_2$ and *A*-$MoS_2$ is a spike signal. Plot of the intensity of the phonon mode at 210 $cm^{-1}$ normalized to the $E^1_{2g}$ mode ($I_{210}/I_{377}$) as a function of the degree of functionalization (b). Plot of the intensity of the phonon mode at 210 $cm^{-1}$ normalized to the $A_{1g}$ mode ($I_{210}/I_{406}$) as a function of the degree of functionalization (c). The dashed lines in (b) and (c) are guides for the eyes. For the intensity ratios shown here, the amplitudes of the Raman peaks were used.

samples, indicating the presence of at least partial 1T- or 1T′-phase in the functionalized samples. These observations are consistent with our XPS, UV/Vis, and DFT calculation results.

Noticeably, a phonon mode at around 210 $cm^{-1}$ strongly increases in intensity in all the functionalized $MoS_2$ samples (Figure 6a). This peak has been observed in many functionalized $MoS_2$ structures,[18,25,38] yet it has not been investigated in most cases. The position of this peak is very close to the first-order scattering of the LA phonon, which is usually activated by structural disorder such as sulfur vacancies and surface adatoms.[37,39–41] A study reported by Roy et al. has pointed out that for single layer $MoS_2$, the peak intensity of LA mode relative to one of first-order Raman modes ($E^1_{2g}$ or $A_{1g}$), is proportional to the density of defects.[39] Inspired by their study, we plotted the intensity of this emerging peak at 210 $cm^{-1}$ relative to the characteristic $E^1_{2g}$ mode ($I_{210}/I_{377}$) and $A_{1g}$ mode ($I_{210}/I_{406}$), as a function of the degree of functionalization (Figure 6b and 7c). The intensity ratios, $I_{210}/I_{377}$ and $I_{210}/I_{406}$, increase with increasing degree of covalent functionalization. This correlation indicates that the activation of the phonon mode at 210 $cm^{-1}$ is associated with functionalization, i.e., the 210 $cm^{-1}$ mode may be used as an indicator to estimate the degree of covalent functionalization of $MoS_2$.

We also performed temperature dependent Raman measurements on *AB*-$MoS_2$ and *BA*-$MoS_2$ powders to monitor the Raman spectra change over the course of the thermolysis of samples. The sample powders were placed on $Si/SiO_2$ wafers, flattened by glass slides and then subjected to Raman measurements under inert atmosphere. For *AB*-$MoS_2$ (Fig-

  

ure S5a), with increasing the temperature, new peaks at 817, 283, and 119 $cm^{-1}$ gradually appear, indicating the formation of $MoO_3$.[42] When the temperature rises above 400 °C, the $E^1_{2g}$ and $A_{1g}$ modes of $MoS_2$ completely vanish, leaving the spectrum dominated by the features of $MoO_3$, suggesting a complete structural transformation upon annealing. Interestingly, the phonon mode at 210 $cm^{-1}$ is preserved over the entire thermolysis process. The intensity ratio of the 210 $cm^{-1}$ mode relative to the characteristic $E^1_{2g}$ mode ($I_{210}/I_{377}$) and $A_{1g}$ mode ($I_{210}/I_{406}$), against temperature (Figure S5b and S5c) reveals two temperature regions: (1) for $T<300$ °C, the intensity ratios slightly increase till reaching a local maximum at around $T=200$ °C, and then decrease to the original value. (2) For $T>300$ °C, the intensity ratios increase. Analogous results were also obtained for *BA*-$MoS_2$ (Figure S6). Several events, such as the detachment of surface tethered functional groups, phase transition from 1T to 2H-$MoS_2$,[1] and the oxidation of $MoS_2$ to $MoO_3$ may take place simultaneously or subsequently with increasing temperature. A detailed study on how these events contribute to the evolution of the Raman spectra will provide a better understanding, however is beyond the scope of this work.

### *Functionalization of mechanically exfoliated $MoS_2$*

We have shown above that the optical properties of $MoS_2$ can be fine-tuned in bulk through step-wise covalent functionalization where both sides of the $MoS_2$ nanoflakes are accessible to electrophiles during the process. Given such a possibility of constructing a bisfunctionalized $MoS_2$ hybrid structure, we have examined whether this strategy can be utilized on substrate supported $MoS_2$ surfaces. To this end, we have used mechanically exfoliated $MoS_2$ (*me*-$MoS_2$) deposited on a $Si/SiO_2$ substrate. Pristine *me*-$MoS_2$ on $Si/SiO_2$ was initially activated by immersing the wafer in *n*-BuLi under inert atmosphere. After rinsed with anhydrous hexane, the activated $MoS_2$ wafer was soaked in the solution of the first electrophile (under inert conditions) followed by a thorough wash with organic solvents and water to give the monofunctionalized $MoS_2$. This wafer was subsequently treated with the second electrophile without further activation, yielding the final adducts (see Supporting Information for details). The topographic information and the thickness profiles of pristine *me*-$MoS_2$@$Si/SiO_2$, *A*-$MoS_2$@$Si/SiO_2$, *B*-$MoS_2$@$Si/SiO_2$, *AB*-$MoS_2$@$Si/SiO_2$, and *BA*-$MoS_2$@$Si/SiO_2$ flakes were monitored using atomic force microscopy (AFM, Figure 7). The AFM image of pristine *me*-$MoS_2$ (Figure 7a) shows a very smooth and flat topography with a lateral dimension of about 2–6 μm, and a thickness of about 4–8 nm, corresponding to 4–8 layers.[43] In comparison, the AFM images of functionalized $MoS_2$ display a rough and corrugated topography. In particular, the protrusions ranging from 10–20 nm are clearly observed in the AFM images of *B*-$MoS_2$@$Si/SiO_2$, *AB*-$MoS_2$@$Si/SiO_2$, and *BA*-$MoS_2$@$Si/SiO_2$. The mechanism of the formation of protrusions on $MoS_2$ nanosheets functionalized using diazonium salts has been discussed in detail in another study,[44] where the generation of chain-like protrusions in those samples can be indicative of the covalent

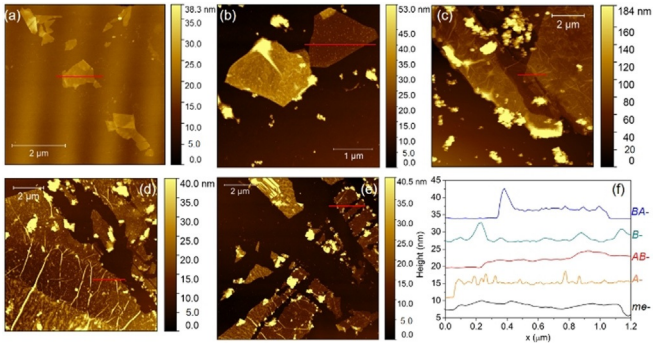


***Figure 7.*** AFM images of pristine *me*-$MoS_2$@$Si/SiO_2$ (a), *A*-$MoS_2$@$Si/SiO_2$ (b), *B*-$MoS_2$@$Si/SiO_2$ (c), *AB*-$MoS_2$@$Si/SiO_2$ (d), and *BA*-$MoS_2$@$Si/SiO_2$ (e) and the corresponding height profiles (f). The height profiles along the red marker in each image were plotted.

attachment of aryl functional groups via diazonium chemistry. Comparing the AFM images of *B*-$MoS_2$@$Si/SiO_2$ and *BA*-$MoS_2$@$Si/SiO_2$ reveals significant fragmentation of nanoflakes in *BA*-$MoS_2$@$Si/SiO_2$ (Figure 7e). This phenomenon was also observed in the SEM image of bulk functionalized sample (Figure 5e, *BA*-$MoS_2$). On the basis of these results, we urge the caution on maintaining an intact $MoS_2$ crystal structure while seeking a high degree of functionalization in future studies. The Raman spectra of pristine *me*-$MoS_2$@$Si/SiO_2$, *A*-$MoS_2$@$Si/SiO_2$, *B*-$MoS_2$@$Si/SiO_2$, *AB*-$MoS_2$@$Si/SiO_2$, and *BA*-$MoS_2$@$Si/SiO_2$ were recorded straightforward under ambient conditions, while the Raman spectrum of activated $MoS_2$ was recorded under inert atmosphere (Figure S7). Importantly, the Raman mode at 210 $cm^{-1}$, which we have previously ascribed to a functionalization related phonon mode, was also detected in all the functionalized samples, confirming the successful covalent functionalization of *me*-$MoS_2$.

### *The key to form bisfunctionalized $MoS_2$*

We have thoroughly characterized the functionalized intermediates and final adducts from two functionalization sequences. TGA-MS, FT-IR, and solid state NMR have shown the presence of hexyl and bromophenyl groups in *AB*-$MoS_2$ but predominantly the bromophenyl group in *BA*-$MoS_2$. XPS has proved that the functional groups were covalently tethered on the surface of $MoS_2$ in all the functionalized samples. The successful covalent modification is also reflected by the prominent feature at 210 $cm^{-1}$ in Raman spectra of functionalized samples (both chemically and mechanically exfoliated $MoS_2$). SEM-EDS corroborates that not only the chemical composition, but also the morphology of *AB*-$MoS_2$ is different from *BA*-$MoS_2$. These results collectively demonstrate that varying the covalent functionalization sequence can result in different hybrid structures. The bisfunctionalized structure can only be achieved through sequence I, alkylation followed by arylation.

To explain why the sequence II, arylation followed by alkylation, cannot lead to the formation of bisfunctionalized

  

product, we set out to evaluate the difference of the number of available binding sites and the reactivity in the two intermediate products: *A*-$MoS_2$ and *B*-$MoS_2$. Our XPS results have shown that the maximum surface coverage (the degree of covalent functionalization) is approximately 30% for both mono- and bisfunctionalized products. In this regard, *A*-$MoS_2$ (degree of functionalization = 21%) is still rich in binding sites, whereas in *B*-$MoS_2$ (degree of functionalization = 32%), the binding sites are already saturated. Therefore, further introducing hexyl groups onto surface of *B*-$MoS_2$ to form the bisfunctionalized product would require the replacement of some surface tethered bromophenyl groups (*B*-) with hexyl groups (*A*-). However, the possibility to displace the bromophenyl groups in *B*-$MoS_2$ with hexyl groups without any other activation treatment seems fairly low. This is in line with preliminary results from our DFT calculation, where the calculated surface bonding distance between functional groups and $MoS_2$ basal plane in *B*-$MoS_2$ is smaller than that in *A*-$MoS_2$. Thus it is reasonable to assume that the bromophenyl groups are more strongly bound to $MoS_2$ than the hexyl groups.

Secondly, the alkylation of $MoS_2$ using alkyl iodides requires negative charge on nanoflakes,[18] however, our previous study[17] and the reference experiment (Figure S8) have proven that the negative charges of *ce*-$MoS_2$ were completely quenched after the functionalization with diazonium salts. To prove the lack of negative charge is the limiting factor for the second step covalent functionalization of *B*-$MoS_2$, we performed a control reaction by reacting re-charged *B*-$MoS_2$ with 1-iodohexane. To this end, the absolutely dried *B*-$MoS_2$ was initially reduced using Na/K alloy,[45] then reacted with 1-iodohexane, yielding the product *B-ac-A*-$MoS_2$ ("*ac*" denotes activation, see Supporting Information for details). The TGA-MS profile of *B-ac-A*-$MoS_2$ (Figure S9) showed the major fragments associated with hexyl groups and phenyl groups, indicating that the both functional groups were attached in *B-ac-A*-$MoS_2$. Comparing the preparation method of *B-ac-A*-$MoS_2$ with that of *BA*-$MoS_2$ revealed the reductive activation of *B*-$MoS_2$ with Na/K alloy was the crucial step to ensure the second step reaction with 1-iodohexane and the formation of bisfunctionalized product. Therefore, the lack of negative charges in *B*-$MoS_2$ was likely the key reason that impeded the second step addition in the original sequence II.

## Conclusion

In conclusion, we have demonstrated an approach to build up a bisfunctionalized $MoS_2$ hybrid structure through successively reacting activated $MoS_2$ with alkyl iodides and diazonium salts. This approach can be utilized to modify both colloidal and substrate supported $MoS_2$ nanosheets. We have discovered distinct reactivity of $MoS_2$ functionalized using alkyl iodide and diazonium salt and only the former allows for subsequent reactions with other electrophiles. By adjusting the reaction sequence and carefully analyzing the reaction intermediates and final adducts, we are able to obtain a series of functionalized $MoS_2$ with varied degrees of functionalization. Raman spectra show a relation between the degree of functionalization and the relative peak intensity of a phonon mode at 210 $cm^{-1}$, which can potentially serve as an indicator to estimate the degree of functionalization. We anticipate that our systematic study on the formation and reactivity of covalently functionalized $MoS_2$ hybrids would encourage the development of new nanomaterials endowed with multiple and customizable functions.

## Acknowledgements

This project has received funding from the European Union's Horizon 2020 research and innovation programme Graphene Flagship under grant agreement No 881603. G. S. Duesberg, C. Bartlam, and T. Stimpel-Lindner thank the EU H2020 under contract No. 829035 (QUEFORMAL) for support. This work was supported in part by the Deutsche Forschungsgemeinschaft (DFG) through the SFB 953 "Synthetic Carbon Allotropes"- B13. Open access funding enabled and organized by Projekt DEAL.

## Conflict of interest

The authors declare no conflict of interest.

**Keywords:** covalent functionalization · hybrid structures · $MoS_2$ · nanosheets · reactivity

[1] G. Eda, H. Yamaguchi, D. Voiry, T. Fujita, M. Chen, M. Chhowalla, *Nano Lett.* **2011**, *11*, 5111 – 5116.
[2] B. Radisavljevic, A. Radenovic, J. Brivio, V. Giacometti, A. Kis, *Nat. Nanotechnol.* **2011**, *6*, 147 – 150.
[3] Y. Guo, W. Zhang, H. Wu, J. Han, Y. Zhang, S. Lin, C. Liu, K. Xu, J. Qiao, W. Ji, Q. Chen, S. Gao, W. Zhang, X. Zhang, Y. Chai, *Sci. Adv.* **2018**, *4*, eaau6252.
[4] J. D. Benck, T. R. Hellstern, J. Kibsgaard, P. Chakthranont, T. F. Jaramillo, *ACS Catal.* **2014**, *4*, 3957 – 3971.
[5] T. F. Jaramillo, K. P. Jørgensen, J. Bonde, J. H. Nielsen, S. Horch, I. Chorkendorff, *Science* **2007**, *317*, 100 – 102.
[6] Y. Wang, J. Mao, X. Meng, L. Yu, D. Deng, X. Bao, *Chem. Rev.* **2019**, *119*, 1806 – 1854.
[7] Y. Huang, J. Guo, Y. Kang, Y. Ai, C. M. Li, *Nanoscale* **2015**, *7*, 19358 – 19376.
[8] K. Lee, R. Gatensby, N. McEvoy, T. Hallam, G. S. Duesberg, *Adv. Mater.* **2013**, *25*, 6699 – 6702.
[9] Q. He, Z. Zeng, Z. Yin, H. Li, S. Wu, X. Huang, H. Zhang, *Small* **2012**, *8*, 2994 – 2999.
[10] Y. Chen, Z. Fan, Z. Zhang, W. Niu, C. Li, N. Yang, B. Chen, H. Zhang, *Chem. Rev.* **2018**, *118*, 6409 – 6455.
[11] Y. Chen, C. Tan, H. Zhang, L. Wang, *Chem. Soc. Rev.* **2015**, *44*, 2681 – 2701.
[12] V. Yadav, S. Roy, P. Singh, Z. Khan, A. Jaiswal, *Small* **2019**, *15*, 1803706.
[13] P. Joensen, R. F. Frindt, S. R. Morrison, *Mater. Res. Bull.* **1986**, *21*, 457 – 461.
[14] J. N. Coleman, M. Lotya, A. O'Neill, S. D. Bergin, P. J. King, U. Khan, K. Young, A. Gaucher, S. De, R. J. Smith, I. V. Shvets, S. K. Arora, G. Stanton, H.-Y. Kim, K. Lee, G. T. Kim, G. S. Duesberg, T. Hallam, J. J. Boland, J. J. Wang, J. F. Donegan, J. C. Grunlan, G. Moriarty, A. Shmeliov, R. J. Nicholls, J. M. Perkins,

  

E. M. Grieveson, K. Theuwissen, D. W. McComb, P. D. Nellist, V. Nicolosi, *Science* **2011**, *331*, 568 – 571.
[15] A. M. van der Zande, P. Y. Huang, D. A. Chenet, T. C. Berkelbach, Y. You, G.-H. Lee, T. F. Heinz, D. R. Reichman, D. A. Muller, J. C. Hone, *Nat. Mater.* **2013**, *12*, 554 – 561.
[16] Y. Yu, G.-H. Nam, Q. He, X.-J. Wu, K. Zhang, Z. Yang, J. Chen, Q. Ma, M. Zhao, Z. Liu, F.-R. Ran, X. Wang, H. Li, X. Huang, B. Li, Q. Xiong, Q. Zhang, Z. Liu, L. Gu, Y. Du, W. Huang, H. Zhang, *Nat. Chem.* **2018**, *10*, 638 – 643.
[17] K. C. Knirsch, N. C. Berner, H. C. Nerl, C. S. Cucinotta, Z. Gholamvand, N. McEvoy, Z. Wang, I. Abramovic, P. Vecera, M. Halik, S. Sanvito, G. S. Duesberg, V. Nicolosi, F. Hauke, A. Hirsch, J. N. Coleman, C. Backes, *ACS Nano* **2015**, *9*, 6018 – 6030.
[18] D. Voiry, A. Goswami, R. Kappera, C. de Carvalho Castro e Silva, D. Kaplan, T. Fujita, M. Chen, T. Asefa, M. Chhowalla, *Nat. Chem.* **2015**, *7*, 45 – 49.
[19] M. Vera-Hidalgo, E. Giovanelli, C. Navío, E. M. Pérez, *J. Am. Chem. Soc.* **2019**, *141*, 3767 – 3771.
[20] S. Bertolazzi, M. Gobbi, Y. Zhao, C. Backes, P. Samorì, *Chem. Soc. Rev.* **2018**, *47*, 6845 – 6888.
[21] X. Chen, A. R. McDonald, *Adv. Mater.* **2016**, *28*, 5738 – 5746.
[22] X. Chen, P. Denninger, T. Stimpel-Lindner, E. Spiecker, G. S. Duesberg, C. Backes, K. C. Knirsch, A. Hirsch, *Chem. Eur. J.* **2020**, *26*, 6535 – 6544.
[23] E. E. Benson, H. Zhang, S. A. Schuman, S. U. Nanayakkara, N. D. Bronstein, S. Ferrere, J. L. Blackburn, E. M. Miller, *J. Am. Chem. Soc.* **2018**, *140*, 441 – 450.
[24] R. Canton-Vitoria, T. Scharl, A. Stergiou, A. Cadranel, R. Arenal, D. M. Guldi, N. Tagmatarchis, *Angew. Chem. Int. Ed.* **2020**, *59*, 3976 – 3981; *Angew. Chem.* **2020**, *132*, 4004 – 4009.
[25] P. Vishnoi, A. Sampath, U. V. Waghmare, C. N. R. Rao, *Chem. Eur. J.* **2017**, *23*, 886 – 895.
[26] M. Cai, F. Zhang, C. Zhang, C. Lu, Y. He, Y. Qu, H. Tian, X. Feng, X. Zhuang, *J. Mater. Chem. A* **2018**, *6*, 138 – 144.
[27] D. O. Li, M. S. Gilliam, X. S. Chu, A. Yousaf, Y. Guo, A. A. Green, Q. H. Wang, *Mol. Syst. Des. Eng.* **2019**, *4*, 962 – 973.
[28] X. Chen, D. McAteer, C. McGuinness, I. Godwin, J. N. Coleman, A. R. McDonald, *Chem. Eur. J.* **2018**, *24*, 351 – 355.
[29] S. J. R. Tan, I. Abdelwahab, Z. Ding, X. Zhao, T. Yang, G. Z. J. Loke, H. Lin, I. Verzhbitskiy, S. M. Poh, H. Xu, C. T. Nai, W. Zhou, G. Eda, B. Jia, K. P. Loh, *J. Am. Chem. Soc.* **2017**, *139*, 2504 – 2511.
[30] J. C. C. Freitas, F. G. Emmerich, G. R. C. Cernicchiaro, L. C. Sampaio, T. J. Bonagamba, *Solid State Nucl. Magn. Reson.* **2001**, *20*, 61 – 73.
[31] V. Alexiev, H. Meyer zu Altenschildesche, R. Prins, T. Weber, *Chem. Mater.* **1999**, *11*, 1742 – 1746.
[32] M. Z. Hossain, M. A. Walsh, M. C. Hersam, *J. Am. Chem. Soc.* **2010**, *132*, 15399 – 15403.
[33] A. Criado, M. Melchionna, S. Marchesan, M. Prato, *Angew. Chem. Int. Ed.* **2015**, *54*, 10734 – 10750; *Angew. Chem.* **2015**, *127*, 10882 – 10900.
[34] X. Chen, N. C. Berner, C. Backes, G. S. Duesberg, A. R. McDonald, *Angew. Chem. Int. Ed.* **2016**, *55*, 5803 – 5808; *Angew. Chem.* **2016**, *128*, 5897 – 5902.
[35] C. Backes, R. J. Smith, N. McEvoy, N. C. Berner, D. McCloskey, H. C. Nerl, A. O'Neill, P. J. King, T. Higgins, D. Hanlon, N. Scheuschner, J. Maultzsch, L. Houben, G. S. Duesberg, J. F. Donegan, V. Nicolosi, J. N. Coleman, *Nat. Commun.* **2014**, *5*, 4576.
[36] X. Zhang, X.-F. Qiao, W. Shi, J.-B. Wu, D.-S. Jiang, P.-H. Tan, *Chem. Soc. Rev.* **2015**, *44*, 2757 – 2785.
[37] S. Jiménez Sandoval, D. Yang, R. F. Frindt, J. C. Irwin, *Phys. Rev. B* **1991**, *44*, 3955 – 3962.
[38] R. Canton-Vitoria, Y. Sayed-Ahmad-Baraza, M. Pelaez-Fernandez, R. Arenal, C. Bittencourt, C. P. Ewels, N. Tagmatarchis, *NPJ 2D Mater. Appl.* **2017**, *1*, 13.
[39] S. Mignuzzi, A. J. Pollard, N. Bonini, B. Brennan, I. S. Gilmore, M. A. Pimenta, D. Richards, D. Roy, *Phys. Rev. B* **2015**, *91*, 195411.
[40] Y. Park, S. Shin, Y. An, J.-G. Ahn, G. Shin, C. Ahn, J. Bang, J. Baik, Y. Kim, J. Jung, H. Lim, *ACS Appl. Mater. Interfaces* **2020**, *12*, 40870—40878.
[41] Q. Qian, Z. Zhang, K. J. Chen, *Langmuir* **2018**, *34*, 2882 – 2889.
[42] L. Seguin, M. Figlarz, R. Cavagnat, J. C. Lassègues, *Spectrochim. Acta Part A* **1995**, *51*, 1323 – 1344.
[43] U. Bhanu, M. R. Islam, L. Tetard, S. I. Khondaker, *Sci. Rep.* **2014**, *4*, 5575.
[44] X. S. Chu, A. Yousaf, D. O. Li, A. A. Tang, A. Debnath, D. Ma, A. A. Green, E. J. G. Santos, Q. H. Wang, *Chem. Mater.* **2018**, *30*, 2112 – 2128.
[45] E. Er, H.-L. Hou, A. Criado, J. Langer, M. Möller, N. Erk, L. M. Liz-Marzán, M. Prato, *Chem. Mater.* **2019**, *31*, 5725 – 5734.

Manuscript received: March 8, 2021
Accepted manuscript online: March 26, 2021
Version of record online: May 7, 2021

  